Detecting beyond-Einstein polarizations of continuous gravitational waves

Maximiliano Isi,[1,*] Alan J. Weinstein,[1,†] Carver Mead,[1,‡] and Matthew Pitkin[2,§]

[1]*California Institute of Technology, Pasadena, California 91125, USA*
[2]*University of Glasgow, Glasgow G12 8QQ, Scotland, United Kingdom*

The direct detection of gravitational waves with the next-generation detectors, like Advanced LIGO, provides the opportunity to measure deviations from the predictions of general relativity. One such departure would be the existence of alternative polarizations. To measure these, we study a single detector measurement of a continuous gravitational wave from a triaxial pulsar source. We develop methods to detect signals of any polarization content and distinguish between them in a model-independent way. We present LIGO Science Run 5 sensitivity estimates for 115 pulsars.

I. INTRODUCTION

Since its introduction in 1915, Einstein's theory of general relativity (GR) has been confirmed by experiment in every occasion [1]. However, GR has not yet been tested with great precision on scales larger than the Solar System or for highly dynamical and strong gravitational fields [2]. Those kinds of rapidly changing fields give rise to gravitational waves (GWs)—self-propagating stretching and squeezing of spacetime originating in the acceleration of massive objects, like spinning neutron stars with an asymmetry in their moment of inertia (e.g., see, Refs. [3,4]).

Although GWs have yet to be directly observed, detectors such as the Laser Interferometer Gravitational Wave Observatory (LIGO) expect to do so in the coming years, giving us a chance to probe GR on new grounds [5,6]. Because GR does not present any adjustable parameters, these tests have the potential to uncover new physics [1]. By the same token, LIGO data could also be used to test alternative theories of gravity that disagree with GR on the properties of GWs.

Furthermore, when looking for a weak signal in noisy LIGO data, certain physical models are used to target the search and are necessary to make any detection possible [2]. Because these are usually based on predictions from GR, assuming an incorrect model could yield a weak detection or no detection at all. Similarly, if GR is not a correct description for highly dynamical gravity, checking for patterns given by alternative models could result in detection where no signal had been seen before.

There exist efforts to test GR by looking at the deviations of the parametrized post-Newtonian coefficients extracted from the inspiral phase of compact binary coalescence

events [7–9]. Besides this, deviations from GR could be observed in generic GW properties such as polarization, wave propagation speed, or parity violation [1,10,11]. Tests of these properties have been proposed that make use of GW burst search methods [12].

In this paper, we present methods to search LIGO-like detector data for continuous GW signals of any polarization mode, not just those allowed by GR. We also compare the relative sensitivity of different model-dependent and -independent templates to certain kinds of signals. Furthermore, we provide expected sensitivity curves for GR and non-GR signals, obtained by means of blind searches over LIGO noise (not actual upper limits).

Section II provides the background behind GW polarizations and continuous waves, while Secs. III and V present search methods and the data analysis procedures used to evaluate sensitivity for detection. Results and final remarks are provided in Secs. V and VI, respectively.

II. BACKGROUND

A. Polarizations

Just like electromagnetic waves, GWs can present different kinds of polarizations. Most generally, metric theories of gravity could allow six possible modes: plus (+), cross (×), vector x (x), vector y (y), breathing (b), and longitudinal (l). Their effects on a free-falling ring of particles are illustrated in Fig. 1. Transverse GWs (+, ×, and b) change the distance between particles separated in the plane perpendicular to the direction of propagation (taken to be the *z* axis). Vector GWs are also transverse, but because all particles in a plane perpendicular to the direction of propagation are equally accelerated, their relative separation is not changed. Nonetheless, particles farther from the source move at later times, hence varying their position relative to points with both different *x-y* coordinates and different *z* distance. Finally, longitudinal GWs change the distance between particles separated along the direction of propagation.

---
[*]misi@ligo.caltech.edu
[†]ajw@ligo.caltech.edu
[‡]carver@caltech.edu
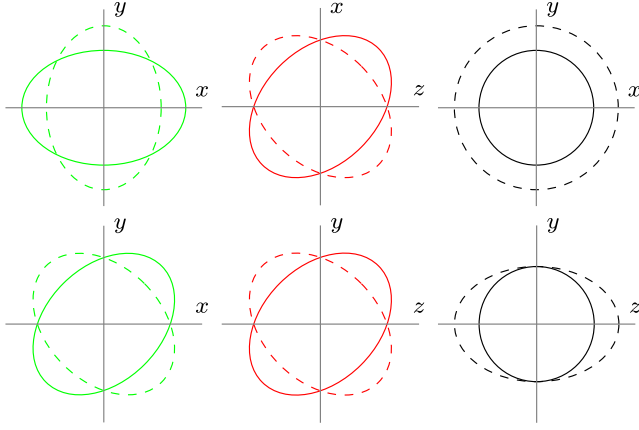[§]matthew.pitkin@glasgow.ac.uk

FIG. 1 (color online).   Illustration of the effect of different GW polarizations on a ring of test particles. Plus (+) and cross (×) tensor modes are in green, vector-x (x) and vector-y (y) modes are in red, and breathing (b) and longitudinal (l) scalar modes are in black. In all of these diagrams, the wave propagates in the z direction [1].

Note that, because of their symmetries, the breathing and longitudinal modes are degenerate for LIGO-like interferometric detectors, so it is enough to just consider one of them in the analysis. Also, this study assumes wave frequency and speed remain constant across modes, which restricts the detectable differences between polarizations to amplitude modulations.

In reality, however, GWs might only possess some of those six components; different theories of gravity predict the existence of different polarizations. In fact, due to their symmetries, + and × are associated with tensor theories, x and y are associated with vector theories, and b and l are associated with scalar theories. In terms of particle physics, this differentiation is also linked to the predicted helicity of the graviton: ±2, ±1, or 0, respectively. Consequently, GR only allows + and ×, while scalar-tensor theories also predict the presence of some extra b component of which the strength depends on the source [1]. Bolder theories might predict the existence of vector or scalar modes *only*, while still being in agreement with all other non-GW tests.

Four-vector gravity (G4v) is one such extreme example [13]. This vector-based framework claims to reproduce all the predictions of GR, including weak-field tests and total radiated power of GWs. However, this theory differs widely from GR when it comes to gravitational wave polarizations. Thus, one of the only ways to test G4v would be to detect a GW signal composed of x and y modes instead of + and ×.

B. Signal

Because of their persistence, continuous gravitational waves (CGWs) provide the means to study GW polarizations without the need for multiple detectors. For the same reason, continuous signals can be integrated over long periods of time, thus improving the likelihood of detection. Furthermore, these GWs are quasi sinusoidal and present well-defined frequencies. This allows us to focus on the amplitude modulation, in which the polarization information is contained.

CGWs are produced by localized sources with periodic motion, such as binary systems or spinning neutron stars [14]. Throughout this paper, we target known pulsars (e.g., the Crab pulsar) and assume an asymmetry in their moment of inertia (rather than precession of the spin axis or other possible, but less likely, mechanisms) causes them to emit gravitational radiation. A source of this type can generate GWs only at multiples of its rotational frequency ν. In fact, it is expected that most power be radiated at twice this value [15]. For that reason, we take the GW frequency, ν_{gw}, to be 2ν. Moreover, the frequency evolution of these pulsars is well known thanks to electromagnetic observations, mostly at radio wavelengths but also in gamma rays.

Simulation of a CGW from a triaxial neutron star is straightforward. The general form of a such signal is

$$h(t) = \sum_p A_p(t; \psi | \alpha, \delta, \lambda, \phi, \gamma, \xi) h_p(t; \iota, h_0, \phi_0, \nu, \dot{\nu}, \ddot{\nu}),$$

(1)

where, for each polarization p, A_p is the detector response (antenna pattern) and h_p a sinusoidal waveform of frequency $\nu_{\mathrm{gw}} = 2\nu$. The detector parameters are λ (longitude), ϕ (latitude), γ (angle of the detector x arm measured from the east), and ξ (the angle between arms). Values for the LIGO Hanford Observatory (LHO), LIGO Livingston Observatory (LLO), and Virgo (VIR) detectors are presented in Table I. The source parameters are α (the right ascension), δ (the declination), ψ (the signal polarization angle), ι (the inclination of the pulsar spin axis relative to the observer's line of sight), h_0 (an overall amplitude factor), ϕ_0 (a phase offset), and ν (the rotational frequency, with $\dot{\nu}$ and $\ddot{\nu}$ its first and second derivatives).

Note that the inclination angle ι is defined as is standard in astronomy, with $\iota = 0$ and $\iota = \pi$, respectively, meaning that the angular momentum vector of the source points toward and opposite of the observer. The signal polarization angle ψ is related to the position angle of the source, which is in turn defined to be the east angle of the projection of the source's spin axis onto the plane of the sky.

TABLE I.   LIGO detectors [16,17].

	LHO	LLO	VIR
Latitude (λ)	46.45° N	30.56° N	43.63° N
Longitude (ϕ)	119.41° W	90.77° W	10.5° E
Orientation (γ)	125.99°	198.0°	71.5°

TABLE II.   Axis polarization (ψ) and inclination (ι) angles for known pulsars [18].

	ψ (deg)	ι (deg)
Crab	124.0	61.3
Vela	130.6	63.6
J1930 + 1852	91	147
J2229 + 6114	103	46
B1706 − 44	163.6	53.3
J2021 + 3651	45	79
J0205 + 6449	90.3	91.6
J0537 − 6910	131	92.8
B0540 − 69	144.1	92.9
J1124 − 5916	16	105
B1800 − 21	44	90
J1833 − 1034	45	85.4

Although there are hundreds of pulsars in the LIGO band, in the majority of cases, we lack accurate measurements of their inclination and polarization angles. The few exceptions, presented in Table II, were obtained through the study of the pulsar spin nebula [18]. This process cannot determine the spin direction, only the orientation of the spin axis. Consequently, even for the best-studied pulsars, ψ and ι are only known modulo a reflection; we are unable to distinguish between ψ and $-\psi$ or between ι and $\pi - \iota$. As will be discussed in Sec. III, our ignorance of ψ and ι must be taken into account when searching for CGWs.

1. Frequency evolution

In Eq. (1), $h_p(t)$ is a sinusoid carrying the frequency modulation of the signal,

$$h_p(t) = a_p \cos \left(\phi(t) + \phi_p + \phi_0^{\mathrm{gw}} \right) \qquad (2)$$

$$\phi(t) = 4\pi \left(\nu t_{\mathrm{b}} + \frac{1}{2} \dot{\nu} t_{\mathrm{b}}^2 + \frac{1}{6} \ddot{\nu} t_{\mathrm{b}}^3 \right) + \phi_0^{\mathrm{em}}, \qquad (3)$$

where t_{b} is the Solar System barycentric arrival time, which is the local arrival time t modulated by the standard Rømer Δ_R, Einstein Δ_E, and Shapiro Δ_S delays [19]:

$$t_{\mathrm{b}} = t + \Delta_R + \Delta_E + \Delta_S. \qquad (4)$$

The leading factor of 4 in the rhs of Eq. (3) comes from the substitution $\nu_{\mathrm{gw}} = 2\nu$. For known pulsars, ϕ_0^{em} is the phase of the radio pulse, while ϕ_0^{gw} is the phase difference between electromagnetic and gravitational waves. Both factors contribute to an overall phase offset of the signal ($\phi_0^{\mathrm{em}} + \phi_0^{\mathrm{gw}}$). This is of astrophysical significance since it may provide insights about the relation between electromagnetic and GW radiation and provide information about the physical structure of the source.

The a_p and ϕ_p coefficients in Eq. (2), respectively, encode the relative amplitude and phase of each

polarization. These values are determined by the physical model. For instance, GR predicts

$$a_+ = h_0(1 + \cos^2 \iota)/2, \qquad \phi_+ = 0, \qquad (5)$$

$$a_\times = h_0 \cos \iota, \qquad \phi_\times = -\pi/2, \qquad (6)$$

while $a_{\mathrm{x}} = a_{\mathrm{y}} = a_{\mathrm{b}} = 0$. On the other hand, according to G4v [13],

$$a_{\mathrm{x}} = h_0 \sin \iota, \qquad \phi_{\mathrm{x}} = -\pi/2, \qquad (7)$$

$$a_{\mathrm{y}} = h_0 \sin \iota \cos \iota, \qquad \phi_{\mathrm{x}} = 0, \qquad (8)$$

while $a_+ = a_\times = a_{\mathrm{b}} = 0$. In both cases, the overall amplitude h_0 can be characterized by [13,15,20]

$$h_0 = \frac{4\pi^2 G}{c^4} \frac{I_{zz} \nu^2}{r} \epsilon, \qquad (9)$$

where r is the distance to the source, I_{zz} is the pulsar's moment of inertia along the principal axis, $\epsilon = (I_{xx} - I_{yy})/I_{zz}$ is its equatorial ellipticity, and, as before, ν is the rotational frequency. Choosing some canonical values,

$$h_0 \approx 4.2 \times 10^{-26} \frac{I_{zz}}{10^{28} \ \mathrm{kg \ m^2}} \left[\frac{\nu}{100 \ \mathrm{Hz}} \right]^2 \frac{1 \ \mathrm{kpc}}{r} \frac{\epsilon}{10^{-6}}, \qquad (10)$$

it is easy to see that GWs from triaxial neutron stars are expected to be relatively weak [21]. However, the sensitivity to these waves grows with the observation time because the signal can be integrated over long periods of time [20].

As indicated in the introduction to this section, we have assumed CGWs are caused by an asymmetry in the moment of inertia of the pulsar. Other mechanisms, such as precession of the spin axis, are expected to produce waves of different strengths and with dominant components at frequencies other than 2ν. Furthermore, these effects vary between theories; for instance, in G4v, if the asymmetry is not perpendicular to the rotation axis, there can be a significant ν component as well as the 2ν component. In those cases, Eqs. (2) and (9) do not hold (e.g., see Ref. [15] for precession models).

2. Amplitude modulation

At any given time, GW detectors are not equally sensitive to all polarizations. The response of a detector to a particular polarization p is encoded in a function $A_p(t)$ depending on the relative locations and orientations of the source and detector. As seen from Eq. (1), these functions provide the amplitude modulation of the signal.

A GW is best described in an orthogonal coordinate frame defined by wave vectors $(\mathbf{w}_x, \mathbf{w}_y, \mathbf{w}_z)$, with $\mathbf{w}_z = \mathbf{w}_x \times \mathbf{w}_y$

being the direction of propagation. Furthermore, the orientation of this wave frame is fixed by requiring that the east angle between $\mathbf{w}_y$ and the celestial north be ψ. In this gauge, the different polarizations act through six orthogonal basis strain tensors [22,23],

$$e_{jk}^+ = \begin{pmatrix} 1 & 0 & 0 \\ 0 & -1 & 0 \\ 0 & 0 & 0 \end{pmatrix}, \tag{11}$$

$$e_{jk}^\times = \begin{pmatrix} 0 & 1 & 0 \\ 1 & 0 & 0 \\ 0 & 0 & 0 \end{pmatrix}, \tag{12}$$

$$e_{jk}^{\mathrm{x}} = \begin{pmatrix} 0 & 0 & 1 \\ 0 & 0 & 0 \\ 1 & 0 & 0 \end{pmatrix}, \tag{13}$$

$$e_{jk}^{\mathrm{y}} = \begin{pmatrix} 0 & 0 & 0 \\ 0 & 0 & 1 \\ 0 & 1 & 0 \end{pmatrix}, \tag{14}$$

$$e_{jk}^{\mathrm{b}} = \begin{pmatrix} 1 & 0 & 0 \\ 0 & 1 & 0 \\ 0 & 0 & 0 \end{pmatrix}, \tag{15}$$

$$e_{jk}^{\mathrm{l}} = \sqrt{2} \begin{pmatrix} 0 & 0 & 0 \\ 0 & 0 & 0 \\ 0 & 0 & 1 \end{pmatrix}, \tag{16}$$

with j, k indexing x, y, and z components. These tensors can be written in an equivalent, frame-independent form:

$$\mathbf{e}^+ = \mathbf{w}_x \otimes \mathbf{w}_x - \mathbf{w}_y \otimes \mathbf{w}_y, \tag{17}$$

$$\mathbf{e}^\times = \mathbf{w}_x \otimes \mathbf{w}_y + \mathbf{w}_y \otimes \mathbf{w}_x, \tag{18}$$

$$\mathbf{e}^{\mathrm{x}} = \mathbf{w}_x \otimes \mathbf{w}_z + \mathbf{w}_z \otimes \mathbf{w}_x, \tag{19}$$

$$\mathbf{e}^{\mathrm{y}} = \mathbf{w}_y \otimes \mathbf{w}_z + \mathbf{w}_z \otimes \mathbf{w}_y, \tag{20}$$

$$\mathbf{e}^{\mathrm{b}} = \mathbf{w}_x \otimes \mathbf{w}_x + \mathbf{w}_y \otimes \mathbf{w}_y, \tag{21}$$

$$\mathbf{e}^{\mathrm{l}} = \sqrt{2}(\mathbf{w}_z \otimes \mathbf{w}_z). \tag{22}$$

If a detector is characterized by its unit arm-direction vectors ($\mathbf{d}_x$ and $\mathbf{d}_y$, with $\mathbf{d}_z$ the detector zenith), its differential-arm response A_p to a wave of polarization p is

$$A_p = \frac{1}{2}(\mathbf{d}_x \otimes \mathbf{d}_x - \mathbf{d}_y \otimes \mathbf{d}_y) : \mathbf{e}^p, \tag{23}$$

where the colon indicates double contraction. As a result, Eqs. (2)–(13) imply

$$A_+ = \frac{1}{2}[(\mathbf{w}_x \cdot \mathbf{d}_x)^2 - (\mathbf{w}_x \cdot \mathbf{d}_y)^2 - (\mathbf{w}_y \cdot \mathbf{d}_x)^2 + (\mathbf{w}_y \cdot \mathbf{d}_y)^2], \tag{24}$$

$$A_\times = (\mathbf{w}_x \cdot \mathbf{d}_x)(\mathbf{w}_y \cdot \mathbf{d}_x) - (\mathbf{w}_x \cdot \mathbf{d}_y)(\mathbf{w}_y \cdot \mathbf{d}_y), \tag{25}$$

$$A_{\mathrm{x}} = (\mathbf{w}_x \cdot \mathbf{d}_x)(\mathbf{w}_z \cdot \mathbf{d}_x) - (\mathbf{w}_x \cdot \mathbf{d}_y)(\mathbf{w}_z \cdot \mathbf{d}_y), \tag{26}$$

$$A_{\mathrm{y}} = (\mathbf{w}_y \cdot \mathbf{d}_x)(\mathbf{w}_z \cdot \mathbf{d}_x) - (\mathbf{w}_y \cdot \mathbf{d}_y)(\mathbf{w}_z \cdot \mathbf{d}_y), \tag{27}$$

$$A_{\mathrm{b}} = \frac{1}{2}[(\mathbf{w}_x \cdot \mathbf{d}_x)^2 - (\mathbf{w}_x \cdot \mathbf{d}_y)^2 + (\mathbf{w}_y \cdot \mathbf{d}_x)^2 - (\mathbf{w}_y \cdot \mathbf{d}_y)^2], \tag{28}$$

$$A_{\mathrm{l}} = \frac{1}{\sqrt{2}}[(\mathbf{w}_z \cdot \mathbf{d}_x)^2 - (\mathbf{w}_z \cdot \mathbf{d}_y)^2]. \tag{29}$$

Accounting for the time dependence of the arm vectors due to the rotation of the Earth, Eqs. (24)–(29) can be used to compute $A_p(t)$ for any value of t. In Fig. 2, we plot these responses for the LHO observing the Crab pulsar, over a sidereal day (the pattern repeats itself every day). Note that the b and l patterns are degenerate ($A_{\mathrm{b}} = -\sqrt{2}A_{\mathrm{l}}$), which means they are indistinguishable up to an overall constant.

Although the antenna patterns are ψ dependent, a change in this angle amounts to a rotation of A_+ into $A_\times$ or of A_{x} into A_{y} and vice versa. If the orientation of the source is changed such that the new polarization is $\psi' = \psi + \Delta\psi$, where ψ is the original polarization angle and $\Delta\psi \in [0, 2\pi]$, it is easy to check that the new antenna patterns can be written [23],

$$A'_+ = A_+ \cos 2\Delta\psi + A_\times \sin 2\Delta\psi, \tag{30}$$

$$A'_\times = A_\times \cos 2\Delta\psi - A_+ \sin 2\Delta\psi, \tag{31}$$

$$A'_{\mathrm{x}} = A_{\mathrm{x}} \cos \Delta\psi + A_{\mathrm{y}} \sin \Delta\psi, \tag{32}$$

$$A'_{\mathrm{y}} = A_{\mathrm{y}} \cos \Delta\psi - A_{\mathrm{x}} \sin \Delta\psi, \tag{33}$$

$$A'_b = A_b, \tag{34}$$

$$A'_l = A_l, \tag{35}$$

and the tensor, vector, and scalar nature of each polarization becomes evident from the ψ dependence.

III. METHOD

A. Data reduction

For some set of interferometric data, we would like to detect CGW signals from a given source, regardless of their polarization, and to reliably distinguish between the
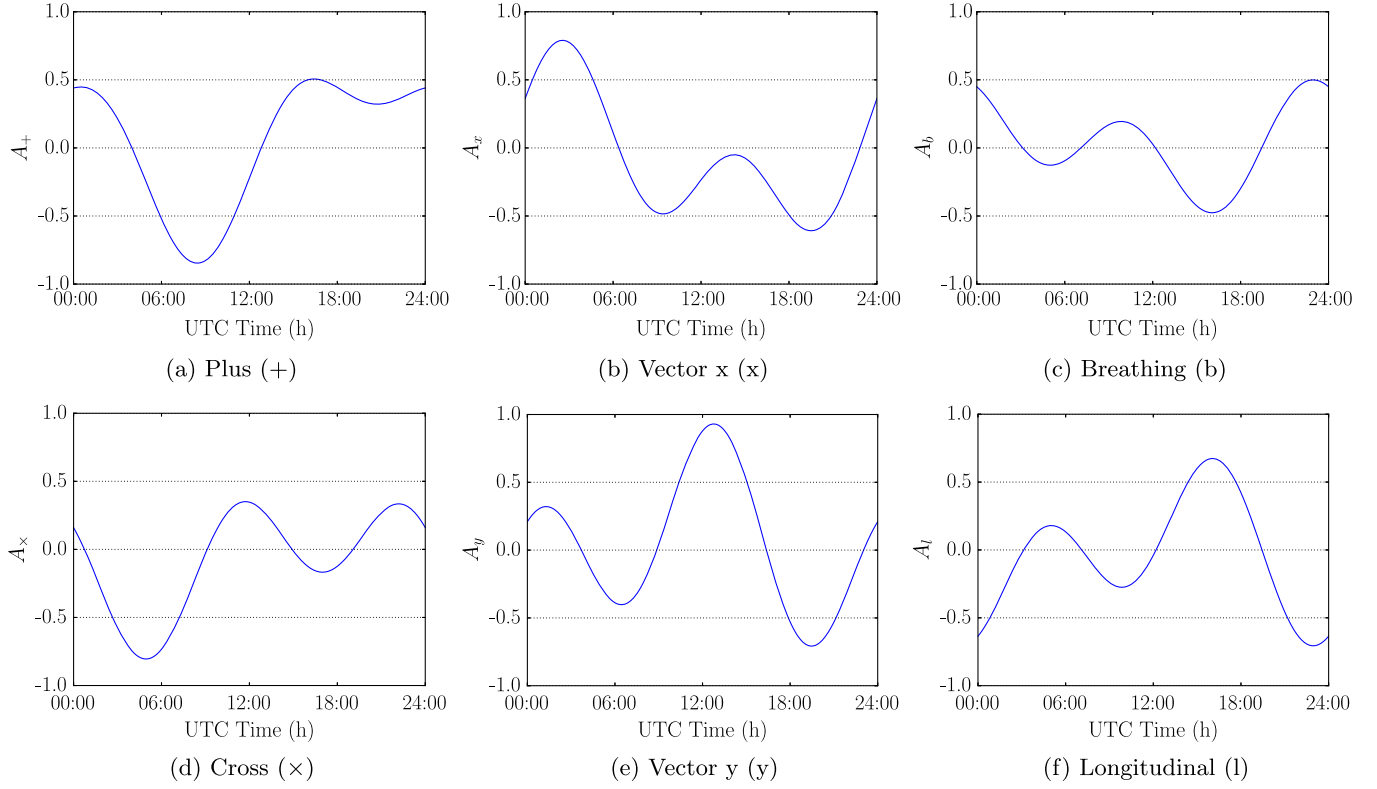
FIG. 2 (color online). LHO response $A_p(t)$, Eq. (23), to different polarizations from the Crab (PSR J0534 + 2200), from 00:00 to 24:00 UTC.

different modes. Because detector response is the only factor distinguishing CGW polarizations, all the relevant information is encoded in the amplitude modulation of the signal. As a result, it suffices to consider a narrow frequency band around the GW frequency, and the data can be considerably reduced following the complex heterodyne method developed in Refs. [24] and [20].

A signal of the form of Eq. (1) can be rewritten as

$$h(t) = \Lambda(t)e^{i\phi(t)} + \Lambda^*(t)e^{-i\phi(t)}, \qquad (36)$$

$$\Lambda(t) = \frac{1}{2}\sum_{p=1}^{5} a_p e^{i\phi_p + i\phi_0} A_p(t), \qquad (37)$$

with $*$ indicating complex conjugation and $\phi(t)$ as given in Eq. (3). Note that we have slightly simplified the notation in Eq. (37) by renaming $\phi_0^{\mathrm{gw}} \rightarrow \phi_0$. Also, the summation is over only five values of p because the breathing and longitudinal polarizations are indistinguishable to the detectors.

The key of the heterodyne method is that, since we can assume the phase evolution is well known from electro-magnetic observations (ephemerides obtained through the pulsar timing package TEMPO2 [19]), we can multiply our data by $\exp\left[-i\phi(t)\right]$ (heterodyning) so that the signal therein becomes

$$h'(t) \equiv h(t)e^{-i\phi(t)} = \Lambda(t) + \Lambda^*(t)e^{-i2\phi(t)} \qquad (38)$$

and the frequency modulation of the first term is removed, while that of the second term is doubled. A series of low-pass filters can then be used to remove the quickly varying term, which enables the down sampling of the data by averaging over minute-long time bins. As a result, we are left with $\Lambda(t)$ only, and Eq. (37) becomes the template of our complex-valued signal. One period of such GR and G4v signals coming from the Crab is presented as seen by LHO in Fig. 3.

From Eq. (38), we see that, in the presence of a signal, the heterodyned and down-sampled noisy detector strain data B_k for the kth minute-long time bin (which can be labeled by GPS time of arrival) are expected to be of the form

$$B_{\mathrm{expected}}(t_k) = \frac{1}{2}\sum_{p=1}^{5} a_p(t_k)e^{i\phi_p + i\phi_0} A_p(t_k) + n(t_k), \qquad (39)$$

where $n(t_k)$ is the heterodyned, averaged complex noise in bin k, which carries no information about the GW signal. As an example, Fig. 4 presents the real part of actual data heterodyned and filtered for the Crab pulsar. We can clearly see already that the data are nonstationary, an issue addressed in Sec. III B and Appendix A.
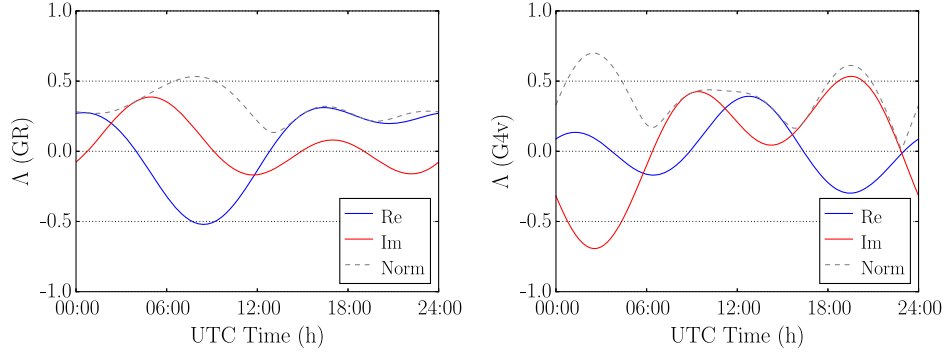
FIG. 3 (color online).   Simulated GR (left) and G4v (right) heterodyned Crab signals as seen by LHO. The templates are generated from Eq. (37) with the model parameters given in Eqs. (5)–(8) and setting $h_0 = 1, \phi_0 = 0$. The solid curves represent the real (blue) and imaginary (red) parts, while the dashed curve corresponds to the complex norm.

B. Search

Given data in this form, we analyze it to obtain the parameters of a signal that would best fit the data and then incorporate the results into the frequentist analysis described in Sec. V. Regressions are performed by minimizing the χ^2 of the system (same as a matched filter). For certain template $T(t_k)$, this is

$$\chi^2 = \sum_{k=0}^{N} [T(t_k) - B(t_k)]^2 / \sigma_k^2, \qquad (40)$$

where σ_k is the estimate standard deviation of the noise in the data at time t_k. In the presence of Gaussian noise, the χ^2 minimization is equivalent to a maximum likelihood analysis.

Any linear template T can be written as a linear combination of certain basis functions f_i, so that $T(t) = \sum_i \tilde{a}_i f_i(t)$ and each $\tilde{a}_i$ is found as a result of minimizing (40). For instance, $T(t_k)$ could be constructed in the from of Eq. (37). In such model-dependent searches, the antenna patterns are the basis set, i.e., $\{f_i\} = \{A_p\}$, and the $\tilde{a}_i$ weights correspond to the $a_p \exp{(i\phi_p)}$ prefactors. (From here on, the tilde denotes the coefficient that is fitted for, rather than its predicted value.)

The regression returns a vector $\tilde{\mathbf{a}}$ containing the values of the $\tilde{a}_i$'s that minimize Eq. (40). These quantities are complex valued and encode the relative amplitude and phase of each contributing basis. From their magnitude, we define the overall *recovered signal strength* to be

$$h_{\text{rec}} = |\tilde{\mathbf{a}}|. \qquad (41)$$

The significance of the fit is evaluated through the covariance matrix C. This can be computed by taking the inverse of $A^T A$, where A is the design matrix of the system (built from the f_i set). In particular, we define the *significance* of the resulting fit [signal signal-to-noise ratio (SNR)] as

$$s = \sqrt{\tilde{\mathbf{a}}^\dagger C^{-1} \tilde{\mathbf{a}}}, \qquad (42)$$

where $\dagger$ indicates Hermitian conjugation.

χ^2–minimizations have optimal performances when the noise is Gaussian. However, although the central limit theorem implies that the averaged noise in Eq. (39) should be normally distributed, actual data are far from this ideal (see Fig. 4). In fact, the quality of the data changes over time, as it is contingent on various instrumental
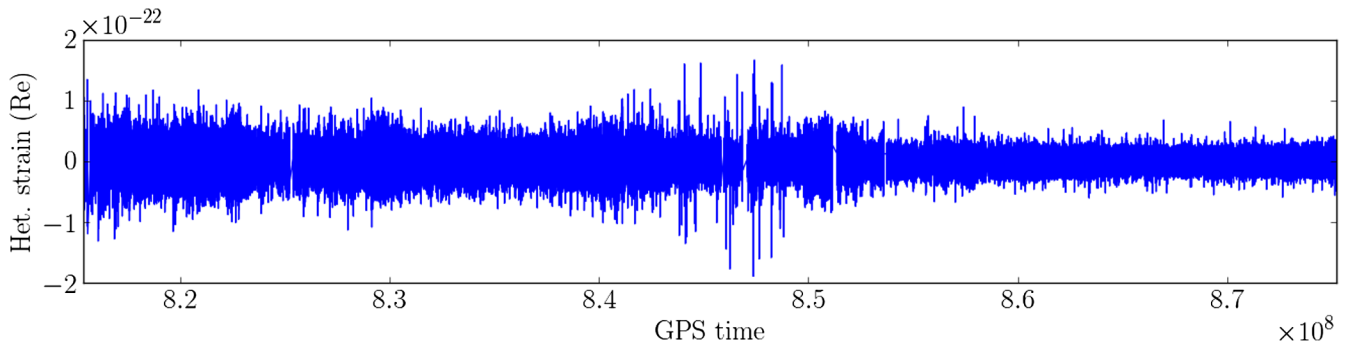

FIG. 4 (color online).   Real part of LIGO Science Run 5 Hanford 4 km detector (H1) minute-sampled data prepared for the Crab spanning approximately two years. A signal in these data would be described by Eq. (39).
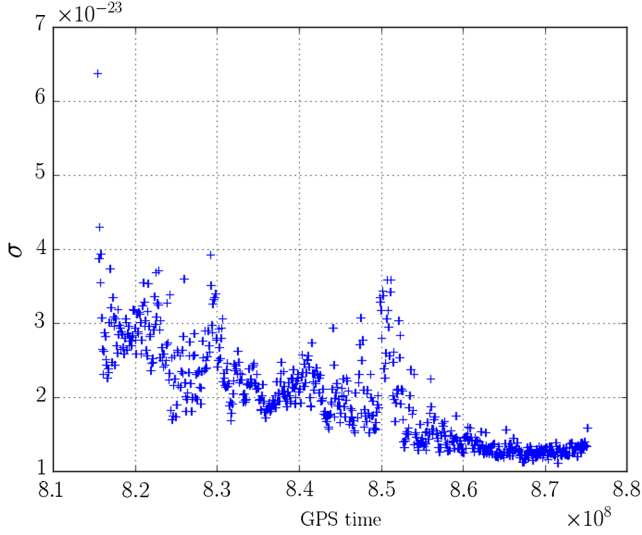
FIG. 5 (color online).   Daily standard deviation of S5 H1 data heterodyned for the Crab pulsar (Fig. 4).

factors. The time series is plagued with gaps and is highly nonstationary. This makes estimating σ_k nontrivial.

As done in regular CGW searches [21], we address this problem by computing the standard deviation for the data corresponding to each sidereal day throughout the data run, rather than for the series as a whole. This method improves the analysis because the data remain relatively stable over the course of a single day, but not throughout longer periods of time (see Appendix A). Furthermore, noisier days have less impact on the fit because σ_k in Eq. (40) will be larger. The evolution of the daily value of the standard deviation for H1 data heterodyned for the Crab pulsar is presented in Fig. 5.

1. Model dependent

In a model-dependent search, a particular physical model is assumed in order to create a template based on Eq. (37). In the case of GR, if ψ and ι are known, it is possible to construct a template with only one complex-valued free parameter $\tilde{h}_0$,

$$T_{GR}(t) = \tilde{h}_0 \frac{1}{2} \left[\frac{1}{2}(1 + \cos^2\iota) A_+(t;\psi) \right.$$
$$\left. + \cos\iota A_\times(t;\psi) e^{-i\pi/2} \right], \quad (43)$$

where the factor of 2 comes from the heterodyne, cf. Eq. (37). Similarly for G4v,

$$T_{G4v}(t) = \tilde{h}_0 \frac{1}{2} \left[\sin\iota e^{-i\pi/2} A_\times(t;\psi) + \sin\iota \cos\iota A_y(t;\psi) \right]. \quad (44)$$

Analogous templates could be constructed for scalar-tensor theories, or any other model. In the former case, there would be a second free parameter to represent the unknown scalar contribution.

However, as mentioned in Sec. II, even in the case of the best-studied pulsars, we know ι only in absolute value. This ambiguity creates the need to use two model-dependent templates like Eqs. (43) and (44): one corresponding to ι and one to $\pi - \iota$. Note that the indeterminacy of ψ is absorbed by the overall phase of $\tilde{h}_0$, so it has no effect on the template. Thus, if the ambiguity in ι is accounted for, the overall signal strength h_0 and the angle ϕ_0 can be inferred directly from the angle and phase of $h_{rec} = \tilde{h}_0$.

In most cases, ψ and ι are completely unknown. It is then convenient to regress to each antenna pattern independently, allowing for two free parameters. This can be done by computing the antenna patterns assuming any arbitrary value of the polarization angle, say $\psi = 0$. Indeed, Eqs. (30)–(35) guarantee that the subspace of tensor, vector, or scalar antenna patterns for *all* ψ is spanned by a pair of corresponding tensor, vector, or scalar antenna patterns assuming any *particular* ψ.

In the case of GR, this means we can use a template,

$$T_{GR}(t) = \tilde{\alpha}_+ A_+(t;\psi = 0)/2 + \tilde{\alpha}_\times A_\times(t;\psi = 0)/2, \quad (45)$$

with two complex weights $\tilde{\alpha}$'s to be determined by the minimization. In the presence of a signal and in the absence of noise, Eqs. (30) and (31) indicate that the values returned by the fit would be a function of the *actual*, unknown ψ and ι,

$$\alpha_+ = a_+(\iota)e^{i\phi_0}\cos 2\psi - a_\times(\iota)e^{i\phi_0 - i\pi/2}\sin 2\psi, \quad (46)$$

$$\alpha_\times = a_\times(\iota)e^{i\phi_0 - i\pi/2}\cos 2\psi + a_+(\iota)e^{i\phi_0}\sin 2\psi, \quad (47)$$

with the $\alpha(\iota)$'s as given in Eqs. (5) and (6).

Again, a (semi-)model-dependent template, like Eq. (45), can be constructed for any given theory by selecting the corresponding antenna patterns to be used as a basis for the regression. For G4v, this would be

$$T_{G4v}(t) = \tilde{\alpha}_x A_x(t;\psi = 0)/2 + \tilde{\alpha}_y A_y(t;\psi = 0)/2 \quad (48)$$

with two complex weights $\tilde{\alpha}$'s to be determined by the minimization. As before, in the presence of a signal and in the absence of noise, Eqs. (32) and (33) indicate that the values returned by the fit would be a function of the actual, unknown ψ and ι:

$$\alpha_x = a_x(\iota)e^{i\phi_0 - i\pi/2}\cos\psi - a_y(\iota)e^{i\phi_0}\sin\psi, \quad (49)$$

$$\alpha_y = a_y(\iota)e^{i\phi_0}\cos\psi + a_x(\iota)e^{i\phi_0 - i\pi/2}\sin\psi. \quad (50)$$

In this case, we cannot directly relate our recovered strength to h_0, and the framework does not allow us to carry

out parameter estimation. The proper way to do that is using Bayesian statistics, marginalizing over the orientation parameters. Since we are mostly interested in quantifying our ability to detect alternative signals rather than estimating source parameters, we do not cover such methods here. However, it would be straightforward to incorporate our generalized likelihoods (as given by our templates) into a full Bayesian analysis (cf. Ref. [20]).

2. Model independent

In a model-independent search, the regression is performed using all five nondegenerate antenna patterns, and the phases between the A_p's are not constrained. Thus,

$$T_{\text{indep}}(t) = \sum_{p=1}^{5} \tilde{a}_p A_p(t). \qquad (51)$$

Because we do not consider any particular model, there is no information about the relative strength of each polarization; hence, the $\tilde{a}_p$'s are unconstrained. Again, Eqs. (30)–(35) enable us to compute the antenna patterns for any value of ψ.

By calculating the necessary inner products, it can be shown that a regression to the *antenna pattern basis*,

$$\{A_+, A_\times, A_\text{x}, A_\text{y}, A_\text{b}\}, \qquad (52)$$

is equivalent to a regression to the *sidereal basis*,

$$\{1, \cos \omega t, \cos 2\omega t, \sin \omega t, \sin 2\omega t\}, \qquad (53)$$

where $\omega = 2\pi/(86164 \text{ s})$ is the sidereal rotational frequency of the Earth. This is an orthogonal basis that spans the space of the antenna patterns. In this basis,

$$T_{\text{indep}}(t) = \sum_{i=1}^{5} \tilde{a}_i f_i(t), \qquad (54)$$

with f_i representing the set in Eq. (53). This is the same basis set used in so-called *5-vector searches* [25].

Because they span the same space, using either basis set yields the same results with the exact same significance, as defined in Eq. (42). Furthermore, the weights obtained as results of the fit can be converted back and forth between the two bases by means of a time-independent coordinate transformation matrix.

A model-independent search is sensitive to all polarizations but is prone to error due to noise when distinguishing between them. It also has more degrees of freedom (compared with a pure-GR template) that can respond to noise fluctuations, resulting in a search that is less sensitive to pure-GR signals. However, the analysis can be followed by model-dependent searches to clarify which theory fits with most significance.

IV. ANALYSIS

We wish to detect any CGW signal originating in a given pulsar, regardless of its polarization in a model-independent way. We can then determine whether the measured polarization content agrees with theoretical predictions. This information can be used to obtain frequentist confidence levels for a potential detection and to generate upper limits for the strength of signals of any polarization potentially buried in the data.

To test the statistical properties of the noisy data filtered through our templates, we produce numerous instantiations of detector noise by taking actual data processed as outlined in Sec. III and reheterodyning over a small band close to the frequency of the original heterodyne. Any true signal in the data stream is scrambled in the process, and what remains is a good
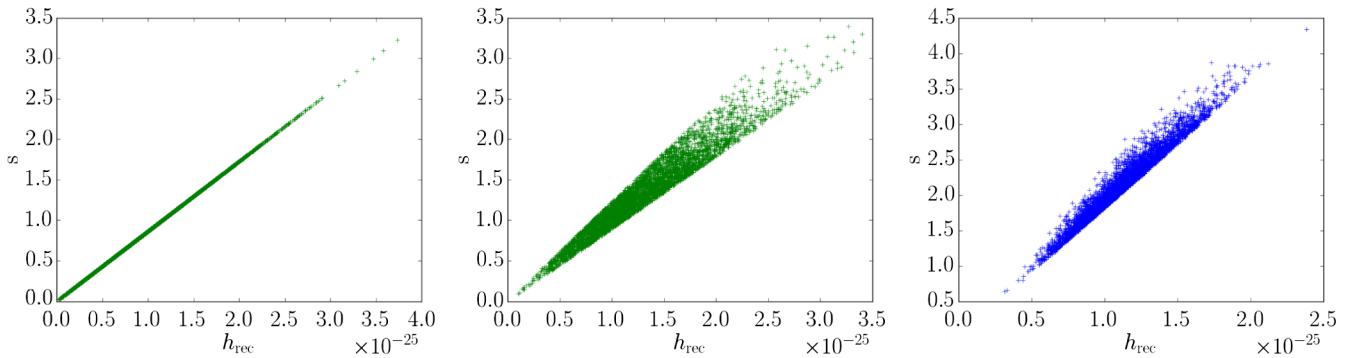

FIG. 6 (color online). Significance, Eq. (42), vs recovered strength, Eq. (41), for searches over 5000 noise-only H1 S5 Crab instantiations using model-dependent Eq. (43) (left), semi-dependent Eq. (45) (center), and model-independent Eq. (54) (right) templates. The model-dependent case assumes *fully* known ι and ψ. Note that the number of degrees of freedom in the regression is manifested in the spread, which is due to noise: templates with a single degree of freedom are less susceptible to noise, and the spread is minimal. The two plots on the left were generated using a GR template, but similar results are obtained for G4v.
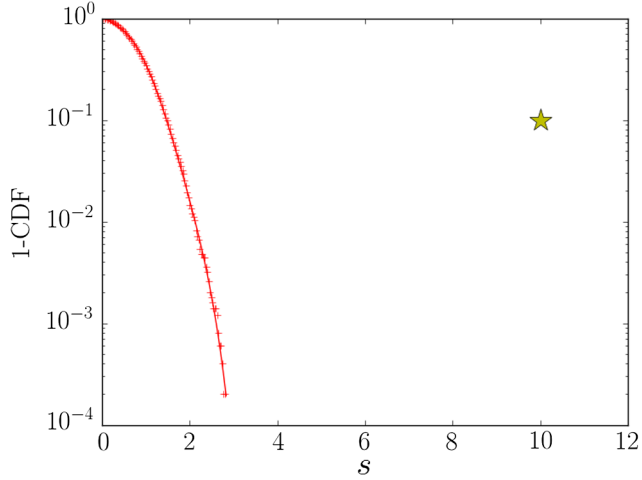
FIG. 7 (color online). Example plot of $p = 1 - \text{CDF}$ vs the recovery significance for a particular template. A loud injection in noise is manifested as an outlier (star) over the noise-only background (red). Note that the injection is plotted arbitrarily at $p = 10^{-1}$.

estimate of the noise. This allows us to perform searches under realistic conditions with or without injections of simulated signals, while remaining blind to the presence of a true signal.

By heterodyning at different frequencies, we are able to generate a large number of instantiations of the data. Because our LIGO Science Run 5 (S5) data sets span roughly 1.9 years and are sampled once per minute, our bandwidth is 8.3×10^{-3} Hz with a lowest resolvable frequency of 1.7×10^{-8} Hz. This means we could

theoretically reheterodyne our data at a maximum of $8.3 \times 10^{-3}/1.7 \times 10^{-8} \approx 4.9 \times 10^{5}$ independent frequencies. In our study, we picked 10^{4} frequencies in the 10^{-7}–10^{-3} Hz range, avoiding the expected signal frequency of $\sim 10^{-5}$ Hz (the period of a sidereal day) and its multiples.

We quantify the results of a particular search by looking at the obtained recovered signal strength, Eq. (41), and significance, Eq. (42). As expected, these two parameters are strongly correlated (Fig. 6). However, the significance is, in the presence of Gaussian noise, a direct indicator of goodness of fit and can be used to compare results from templates with different numbers of degrees of freedom.

By performing searches on multiple instantiations of noise-only data, we construct cumulative distribution function (CDF) probability plots showing the distribution of the recovered signal strength, Eq. (41), and significance, Eq. (42), corresponding to a given template. Such plots give the probability that the outcome of the regression is consistent with noise (i.e., provide p values). As shown in Fig. 7, an instantiation that contains a loud injected signal becomes manifest in this plot as an outlier. This sort of plot can also be used when searching for an actual signal in the data—namely, when looking at the original, non-reheterodyned series. In that case, the $1 - \text{CDF}$ curve can be extrapolated or interpolated to find the p value corresponding to the significance with which the injection was recovered.

After injecting and retrieving increasingly loud signals with a given polarization content in different background instantiations, we produce plots of recovered strength vs
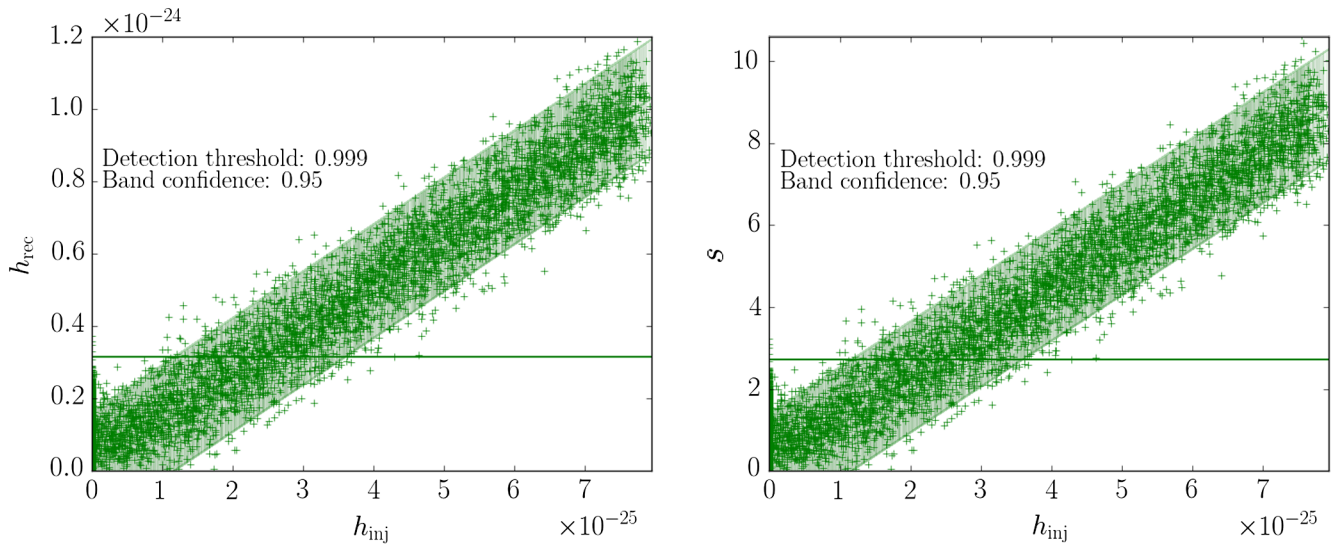

FIG. 8 (color online). Neyman plot of recovered signal strength h_{rec} (left) and significance s (right) vs injected strength h_{inj}. In this case, GR signals are recovered with GR templates, but results are qualitatively the same with G4v injections recovered with G4v templates or either kind of injection recovered with model-independent templates. The collection of points at $h_{\text{inj}} = 0$ are noise only, and the detection threshold (horizontal line) is placed above $\alpha_{\text{n}} = 99.9\%$ of them. The shaded band includes $\alpha_{\text{b}} = 95\%$ of the data points above the threshold, and it is centered on their best-fit line. The fit forced a null y intersect.

injected strength (h_{rec} vs h_{inj}) and significance vs injected strength (s vs h_{inj}). Recall that injections are of the form of Eqs. (43) and (44). Examples of such plots are presented in Fig. 8. These plots, and corresponding fits, can be used to assess the sensitivity of a template to certain type of signal, define thresholds for detection and produce confidence bands for recovered parameters. (In the frequentist literature, these plots are sometimes referred to as *Neyman constructions* [26].)

We define a horizontal *detection threshold* line above an arbitrary fraction α_n (e.g., $\alpha_n = 99.9\%$) of noise-only points (i.e., points with $h_{inj} = 0$, but $h_{rec} \neq 0$) so that data points above this line can be considered detected with a p value of $p = 1 - \alpha_n$ (e.g., $p = 0.1\%$). For a particular template, this fractional threshold can be directly translated into a significance value s_{α_n} (e.g., $s_{99.9\%} = 2.5$). The sensitivity of the template is related to the number of injections recovered with a significance higher than s_{α_n}.
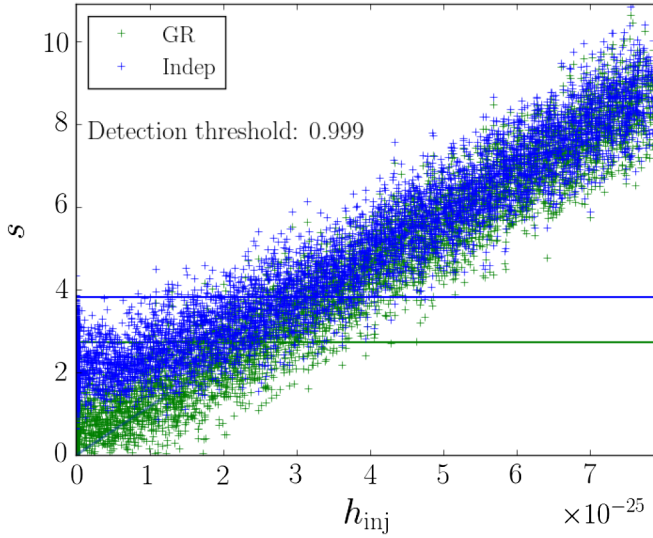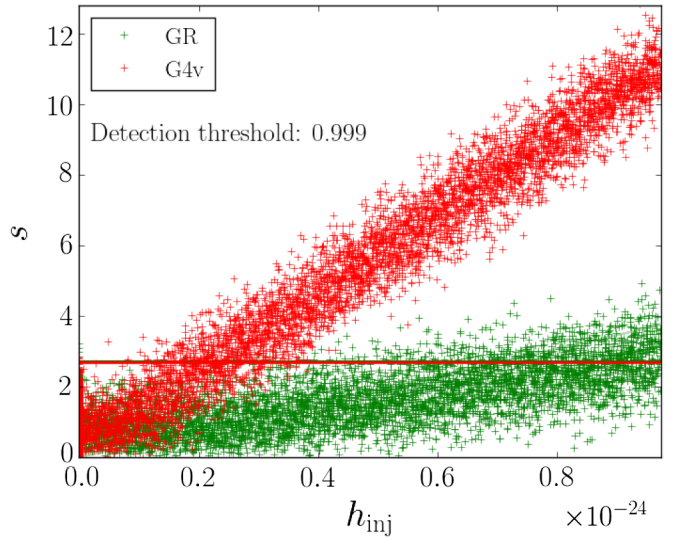

(a) GR injections recovered with GR template (green), eq. (45), and model independent (blue), eq. (54).
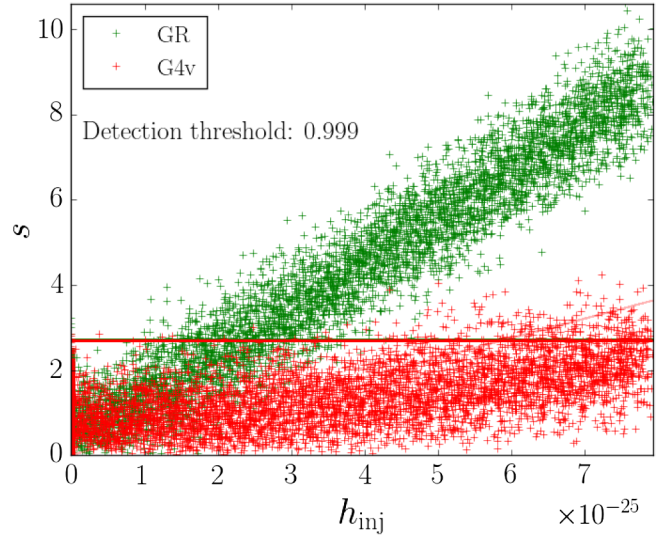
(b) GR injections recovered with GR template (green), eq. (45), and G4v template (red), eq. (48).
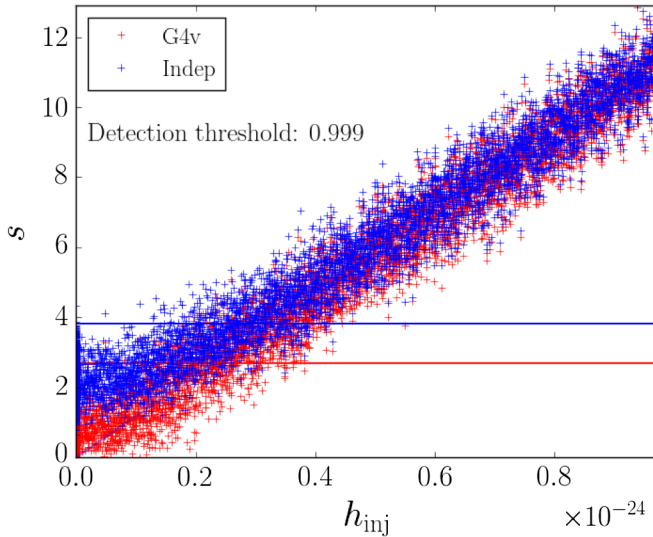
(c) G4v injections recovered with G4v template (red), eq. (48), and model independent (blue), eq. (54).

(d) G4v injections recovered with G4v template (red), eq. (48), and GR template (green), eq. (45).

FIG. 9 (color online). GR (top) and G4v (bottom) injection results of the search over LIGO S5 H1 data heterodyned for the Crab pulsar. Plots show significance, Eq. (42), vs injected strength. Color corresponds to the template used for recovery: GR, green; G4v, red; and model independent, blue. This particular search was performed using 10^4 instantiations, half of which contained injections using the values of ι and ψ given in Table I. The model-dependent templates assumed the same ι as the injections. Horizontal lines correspond to a detection threshold $\alpha_n = 99.9\%$.

Therefore, for a given α_n, a lower s_{α_n} means higher sensitivity to true signals.

For the results of each template, the fractional threshold α_n can also be associated to a strain value. We define this to be the loudness of the minimum injection detected above this threshold with some arbitrary *upper-limit confidence* α_{up}. This value can be determined from the s vs h_{inj} plot by placing a line parallel to the best fit but to the right of a fraction α_{up} of all data points satisfying $0 < h_{inj}$. The intersection of this line with the α_n line occurs at $h_{inj} = h_{min}^{\alpha_{up}}$, which is the strain value above which we can have α_{up} confidence that a signal will be detected (i.e., recovered with significance $s > s_{\alpha_n}$).

We refer to $h_{min}^{\alpha_{up}}$ as the *expected sensitivity* or *strain detection threshold at* α_n. This value allows not only for the definition of upper limits for the presence of signals but also the comparison of different model-dependent and -independent templates. See Fig. 9(b) for a juxtaposition of the results of matching and nonmatching model-dependent templates for the case of the Crab pulsar.

The efficiency of a template is also quantified by the slope of the h_{rec} vs h_{inj} best-fit line, which should be close to 1 for a template that matches the signal. We perform this fit by taking into account only points above the α_n line and forcing the y intersect to be null. The deviations from this fit are used to produce confidence intervals for the recovered strength. This is done by defining a band centered on the best-fit line and enclosing an arbitrary fraction α_b (e.g., $\alpha_b = 95\%$) of the data points, corresponding to the confidence band placed around best-fit line. The intersection between this band and a horizontal line at some value of h_{rec} yields a confidence interval for the true strength with α_b confidence. Note that deviations above and below the best-fit line are taken independently to obtain asymmetric confidence intervals. The same analysis can be done on the s vs h_{inj} plots, taking into account proper scaling of the best-fit slope.

In general, when performing injections, we pick parameters with a uniform distribution over the uncertainty ranges of location and orientation values obtained from the Australia Telescope National Facility Pulsar Catalog [27]. When there is no orientation information, we must draw ψ and ι from the ranges $[-\pi/2, \pi/2]$ and $[0, 2\pi]$, respectively. Note that standard searches consider tensor signals (2ψ dependent) only and therefore assume $\psi \in [-\pi/4, \pi/4]$; however, a bigger range must be used when taking into account vector signals (ψ dependent). The reason these ranges need not cover the full $[0, \pi]$ range is that a change in ψ of $\pi/2$ for tensor and π for vector signals is equivalent to a change of signal sign. Therefore, this is taken care of by varying the overall phase $\phi_0 \in [0, \pi]$.

We tested the aforementioned methods on LIGO data taken by the Hanford and Livingston detectors over S5. During this run, which took place from November 2005 through September 2007 (GPS times 815155213–875232014), the three LIGO detectors operated in data-taking mode at design sensitivity, collecting a year of coincident detector data. The root-mean-square strain noise of the instrument reached values as low as 3×10^{-22} for bands of 100 Hz over the most sensitive frequencies [28]. LIGO S5 data have been recently released to the public and are accessible online through the LIGO Open Science Center [29].

In particular, we looked at data for 115 pulsars, obtained by reducing S5 H1, H2, and L1 strain data as outlined in Sec. III B. But for the inclusion of PSR J0024-72040 and the exclusion of PSR J2033 + 17 and Vela, these are the same heterodyned time series analyzed in Ref. [21]. However, that study presented Bayesian upper limits to the presence of GR signals and did not consider alternative polarizations.

V. RESULTS

Here, we present the results of a study of the signal sensitivity of the analysis procedure described in Sec. V, using the data described at the end of section. We perform a "closed box" analysis, using only reheterodyned data, which are insensitive to the presence of actual signals, and simulated signal injections. A full "open box" analysis, using Bayesian methods to produce model-dependent and model-independent signal detection confidence bands or upper limits, is in preparation.

In particular, we produced 10^4 reheterodyned instantiations of data for each pulsar by picking linearly spaced frequencies in the 10^{-7}–10^{-3} Hz range (cf. Sec. V). Half of those were injected with simulated signals of increasing strength. The data were then analyzed with each template (GR, G4v, and model independent), producing plots like those in Fig. 8. For the Crab pulsar, since the source orientation information is known, the full model-dependent templates, Eqs. (43) and (44), were used; otherwise, the semi-model-dependent templates, Eqs. (45) and (48), were used. The whole process was carried out for both GR and G4v injections. In all cases, we set $\alpha_n = 99.9\%$ and $\alpha_{up} = 95.0\%$.

A. Crab pulsar

Results for searches over H1 S5 data prepared for the Crab pulsar ($\nu = 30.22$ Hz, $\nu_{GW} = 60.44$ Hz) are

TABLE III. Summary of expected sensitivity for the Crab pulsar S5 H1 searches ($\alpha_n = 99.9\%$, $\alpha_{up} = 95.0\%$). Rows correspond to injection type, and columns correspond to the search template. The rotational frequency of the Crab is $\nu = 30.22$ Hz, and therefore $\nu_{GW} = 60.44$ Hz.

	GR	G4v	Independent
GR	3.41×10^{-25}	7.49×10^{-25}	4.20×10^{-25}
G4v	8.90×10^{-25}	3.30×10^{-25}	4.15×10^{-25}

(a) GR slope
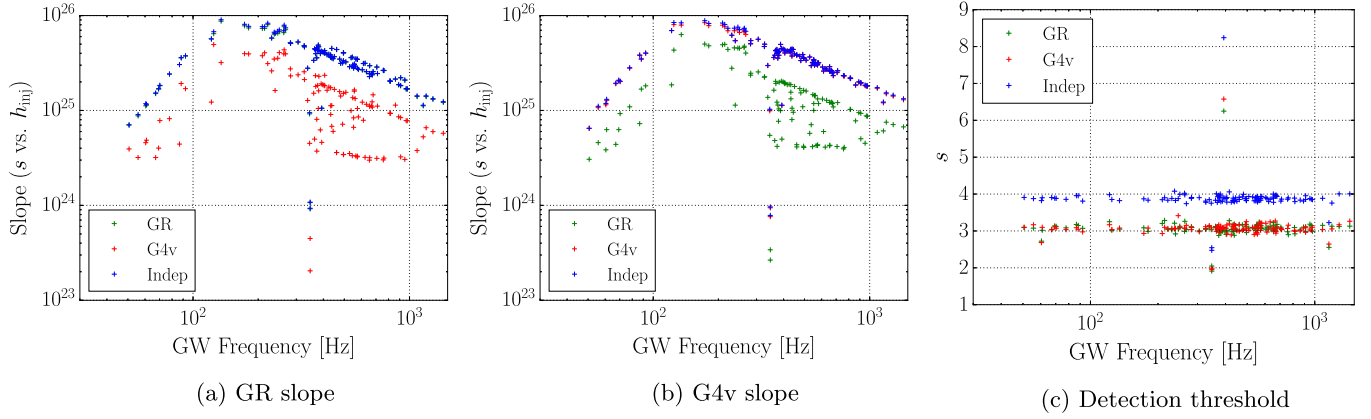
(b) G4v slope

(c) Detection threshold

FIG. 10 (color online). Slope of the s vs h_{inj} best-fit line (left and center) and significance detection threshold at $\alpha_n = 99.9\%$ (right) vs GW frequency and for GR and G4v injections on S5 H1 data for 115 pulsars. Color corresponds to the search template: GR, green; G4v, red; and model independent, blue. Note that for both kinds of injections the model-independent points overlap the matching template.

presented in Fig. 9. The results using templates matched to the injections are compared to those of the model-independent (left) and nonmatching templates (right). The expected sensitivities, as defined in Sec. V, for each injection template and search model are provided in Table III. Recall that the Crab is a special case, since its orientation in the sky is well known, which enables us to use full model-dependent templates, Eqs. (43) and (44). However, searches for actual signals would still have to make use of two templates for each theoretical model because of the ambiguity in ι described in Sec. II B. To avoid doing this, a semi-model-dependent or model-independent search could be carried out instead.

A number of interesting observations can be drawn from Fig. 9 and Table III. As inferred from the values of h_{min}, the model-independent template is roughly 25% less sensitive than the matching one, regardless of the theory assumed when making injections. This is understood by the presence of 4 extra degrees of freedom in the model-independent template, compared to the single tunable coefficient in the full model-dependent one. If instead the semi-model-dependent template with 2 degrees of freedom is used, the improvement with respect to the model-independent search goes down to 15%. In any case, the accuracies of matching and model-independent searches,

given by the width of the confidence bands, are almost identical.

Model-dependent templates are significantly less sensitive to nonmatching signals. Table III indicates that model-dependent templates are 120%–170% less sensitive to nonmatching signals than their matching counterpart. A consequence of this is the existence of a range of signals that would be detected by templates of one theory but not the other [see Figs. 9(b) and 9(d)]. This is particularly interesting, given that previous LIGO searches assume GR to be valid and use a template equivalent to Eq. (43). Therefore, our results suggest it is possible that those searches might have missed fully non-GR signals buried in the data (see Sec. VI for further discussion).

B. All pulsars

The Crab pulsar is only one of the 115 sources we analyzed. The results, presented in Figs. 10(a) and 10(b) generally confirm the observations anticipated from the Crab. While model-independent searches are of the same accuracy as matching semi-model-dependent ones, their strain detection threshold is louder due to the extra degrees of freedom [Fig. 10(c)]. Consequently, model-independent templates demand a higher significance to be able to distinguish a signal from noise. The detection thresholds for GR and G4v templates are of the same magnitude, since both have the same number of degrees of freedom. Among all 115 pulsars, the sources with best expected sensitivities to GR and G4v signals were PSR J1603-7202 and PSR J1748-2446A, respectively (see Table IV).

The key results of our study are summarized in Fig. 11 for H1 and Fig. 12 for L1. These plots present the expected sensitivity (strain detection threshold at $\alpha_n = 99.9\%$ with $\alpha_{up} = 95.0\%$ confidence) vs GW frequency ($\nu_{GW} = 2\nu$). The outliers seen in Figs. 10–12 correspond

TABLE IV. Best expected sensitivities for S5 H1 searches ($\alpha_n = 99.9\%$, $\alpha_{up} = 95.0\%$). Rows correspond to injection type, and columns correspond to pulsar name (PSR), rotation frequency (ν), and strain detection threshold for matching dependent (h_{dep}) and independent (h_{indep}) templates.

|	PSR	ν (Hz)	h_{dep}	h_{indep}
GR	J1603-7202	67.38	4.77×10^{-26}	5.53×10^{-26}
G4v	J1748-2446A	86.48	4.96×10^{-26}	5.81×10^{-26}
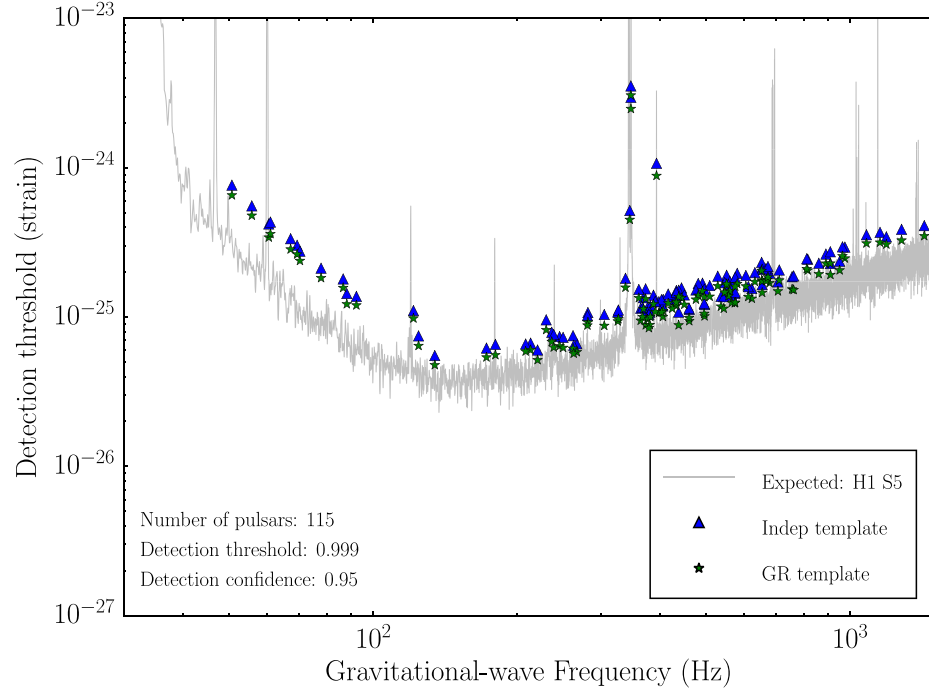
(a) GR injections
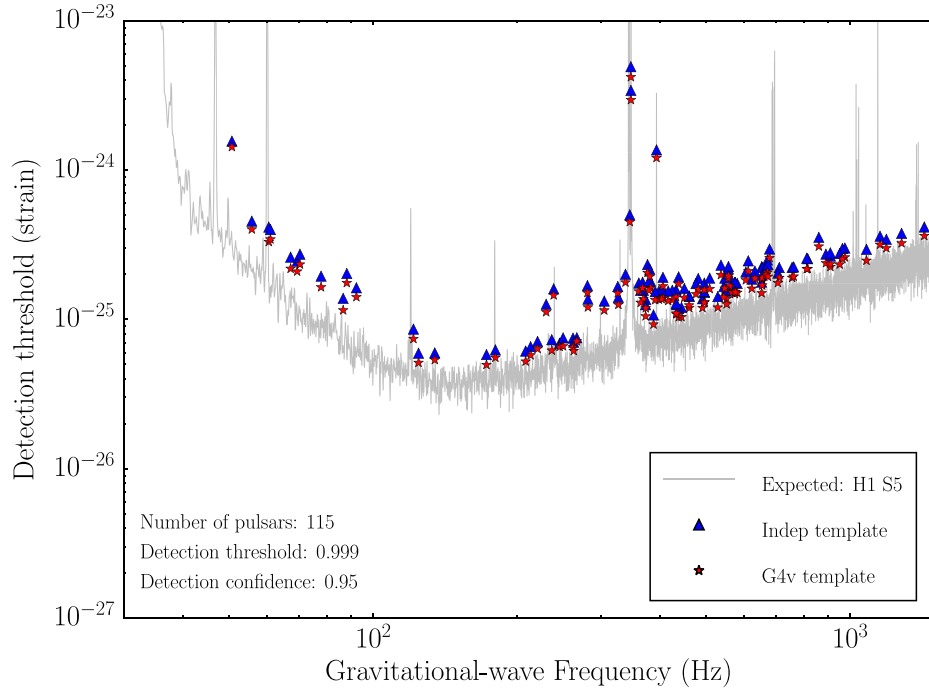
(b) G4v injections

FIG. 11 (color online). S5 H1 expected sensitivity (strain detection threshold at $\alpha_n = 99.9\%$ with $\alpha_{up} = 95.0\%$ confidence) vs GW frequency for 115 pulsars. Color corresponds to the search template: GR, green; G4v, red; and model independent, blue. The gray line is the anticipated sensitivity of a standard Bayesian search, Eq. (55).

to pulsars of which the values of ν_{GW} are very close to instrumental noise spectral lines associated with violin resonances of the detectors test mass pendulum suspensions.

For the matching or model-independent templates, the resulting data points trace the noise curve of the instrument; however, due to the long integration time, we are able to detect signals below LIGO's standard strain noise. The gray
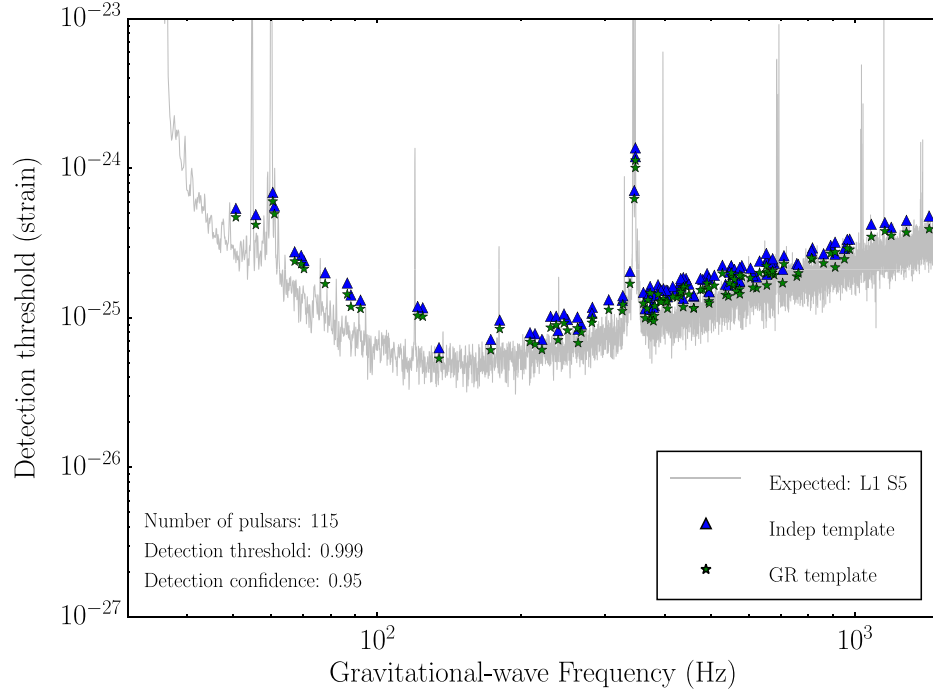
(a) GR injections
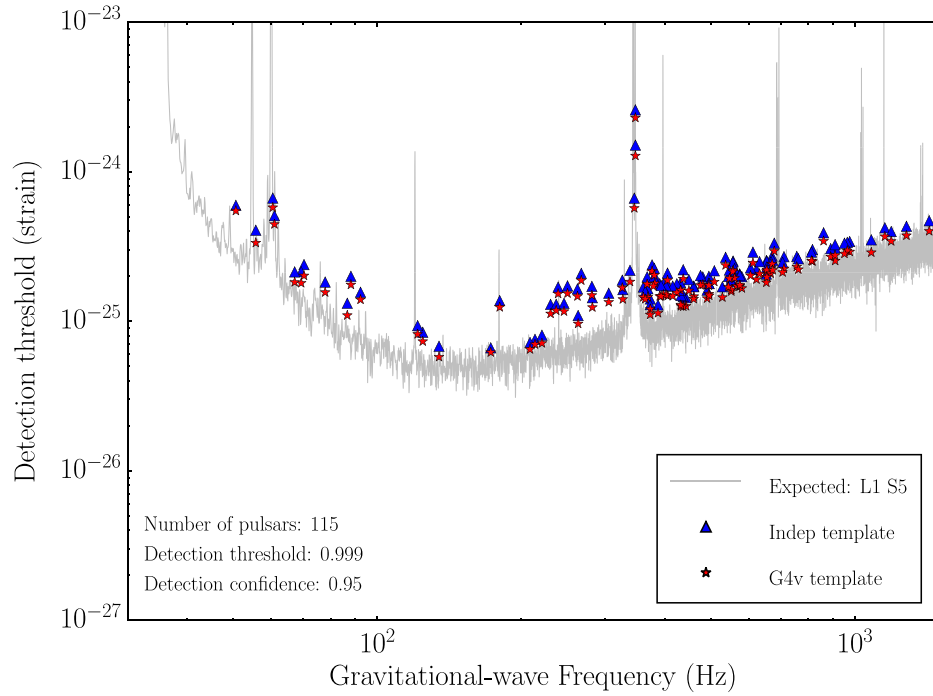
(b) G4v injections

FIG. 12 (color online). S5 L1 expected sensitivity (strain detection threshold at $\alpha_n = 99.9\%$ with $\alpha_{up} = 95.0\%$ confidence) vs GW frequency for 115 pulsars. Color corresponds to the search template: GR, green; G4v, red; and model independent, blue. The gray line is the anticipated sensitivity of a standard Bayesian search, Eq. (55).

curve shown in Figs. 11 and 12 represents the expected sensitivity of a regular Bayesian GR search (e.g., Ref. [21]). This is proportional to the amplitude spectral density of the detector and inversely proportional to the square root of the observation time. The particular empirical relationship used to generate the curve in Figs. 11 and 12 is

$$\langle h_{\min} \rangle = 10.8\sqrt{S_n(f)/T}, \tag{55}$$

TABLE V. Average sensitivity ratios $\langle\rho\rangle$, Eq. (56), for S5 H1 (first value) and S5 L1 (second value) searches. Rows correspond to injection type, and columns correspond to the search template.

	GR		G4v		Independent	
GR	16.11	14.65	58.53	51.89	18.83	17.15
G4v	61.21	55.06	18.42	16.76	21.24	19.32

TABLE VI. Crab sensitivity ratio ρ, Eq. (56) evaluated at the Crab's GW frequency, for S5 H1 (first value) and S5 L1 (second value) searches. Rows correspond to injection type, and columns correspond to the search template.

	GR		G4v		Independent	
GR	20.75	10.40	45.52	27.15	25.54	11.94
G4v	54.06	20.30	20.07	9.96	25.21	11.52

with $S_n(f)$ the noise power spectral density and T the total observation time (527 days for S5 H1 and 405 days for S5 L1) [20]. This formula enables the comparison of the methods presented here with the expected performance of standard Bayesian searches.

By the same token, we can define a figure of merit ρ for our searches by the ratio

$$\rho(\nu_{\text{GW}}) = h_{\min}/\sqrt{S_n(\nu_{\text{GW}})/T}. \tag{56}$$

The average of this value over all pulsars, $\langle\rho\rangle$, can be semiquantitatively compared to the 10.8 prefactor in Eq. (55). The equivalence is not direct because, besides the intrinsic differences between Bayesian and frequentist approaches, Eq. (55) was obtained by averaging the results of 4000 simulated searches [20], while we include just the 115 pulsars at hand. The values of $\langle\rho\rangle$ for our S5 H1 and L1 analyses are presented in Table V and Fig. 13. The specific values for the Crab pulsar are shown in Table VI. A smaller ρ indicates better performance.
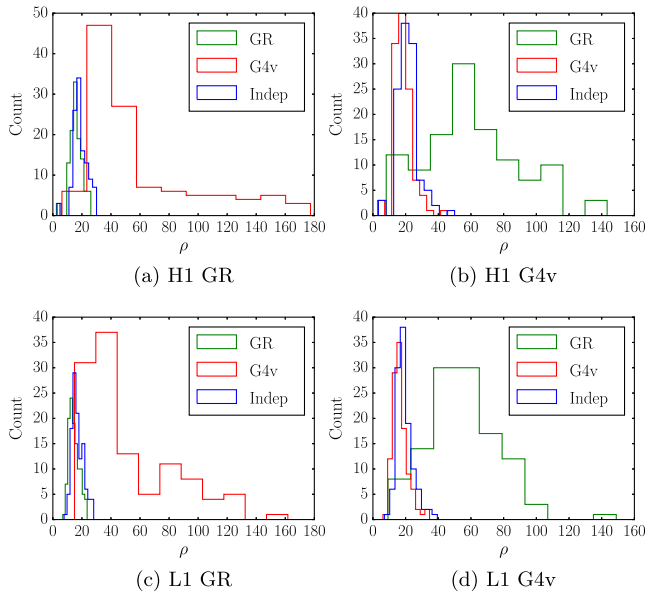

FIG. 13 (color online). Histograms of the figure of merit ρ, Eq. (56), for our searches over S5 H1 (top) and L1 (bottom) data sets with GR (left) and G4v (right) injections, corresponding to 115 pulsars. Color corresponds to the search template: GR, green; G4v, red; and model independent, blue.

As mentioned above, the remarks made about the Crab pulsar hold for most other sources, except that detectability is slightly lower because orientation parameters are unknown. In all cases, the matching template is the best at recovering signals, followed closely by the model-independent one. Searches that assume the incorrect model are substantially less efficient, and their $h_{\min}$ vs ν_{GM} curves do not follow the instrumental noise line. This is reflected, for instance, by the figures of merit presented in Table V.

VI. CONCLUSIONS

We have developed novel model-independent methods to search for CGW signals coming from targeted sources in LIGO-like interferometric data. These searches are able to detect signals of *any* polarization content with high significance.

To test our methods in the presence of realistic noise conditions, we implemented a procedure to produce thousands of noise-only instantiations from actual data. We then proceeded by injecting and retrieving increasingly loud signals of different polarization content.

We studied 115 pulsars using S5 data from the LIGO Hanford and Livingston detectors. Although the methods are general, we restricted our study to two theories that predict starkly different GW polarization contents (GR and G4v).

Our results indicate that assuming the wrong theoretical model greatly reduces the sensitivity of a search to signals buried in the data. Yet, our model-independent searches are almost as effective as the model-dependent templates that match the kind of signal injected (i.e., when the models used for the injection and search are the same). This means that our model-independent templates can be used to find signals of any polarizations without additional computational requirements.

We are able to reach sensitivities comparable to previous studies, although slightly worse than those presented in Ref. [21]. This is probably due to our making use of a single detector and to differences between frequentist and Bayesian approaches.

We have shown that, for some combinations of detectors, sources, and signal strengths, G4v signals are invisible to GR templates and vice versa. Therefore, it is possible that, if GWs are composed uniquely of vector modes, previous
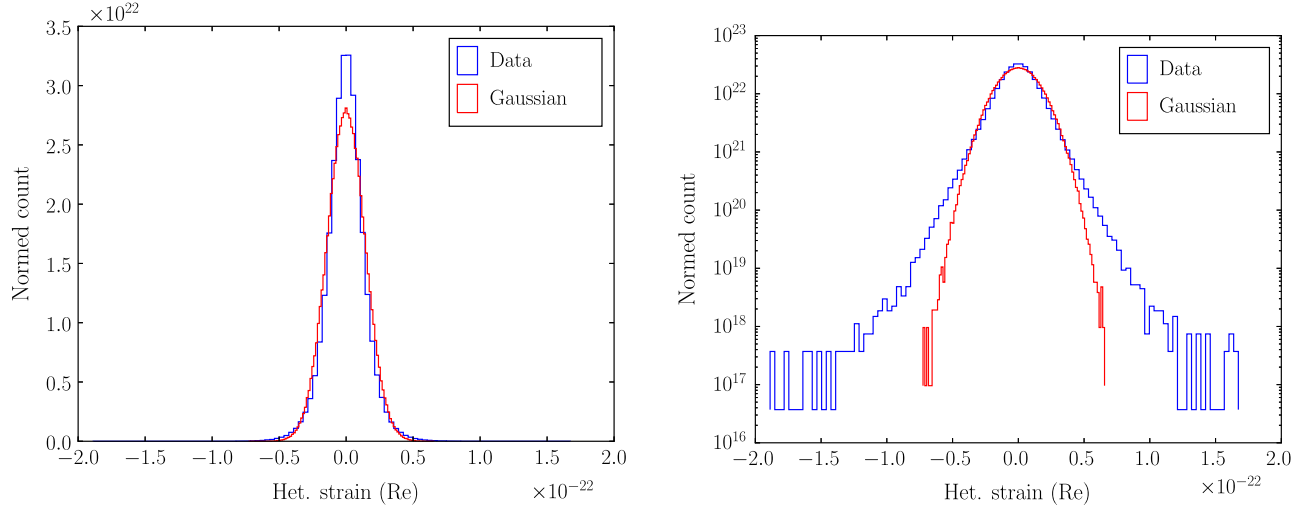
FIG. 14 (color online). Normalized histogram of the real part of S5 H1 data heterodyned for the Crab in linear (left) and logarithmic *y* scales. A Gaussian curve with the same standard deviation is plotted in red for comparison.

LIGO searches, which assume GR, may have missed their signals.

It is clear that the next step in this study consists of incorporating our model-independent templates into the Bayeasian machinery used in standard LIGO Scientific Collaboration searches. This will allow us to properly marginalize over all nuisance parameters and to produce multidetector model-dependent and model-independent signal detection confidence bands or upper limits. We will also employ methods to constrain other theories (e.g., scalar tensor) in the event of a model-independent detection.

ACKNOWLEDGMENTS

APPENDIX: STATISTICAL PROPERTIES OF LIGO DATA

The χ^2 minimization is equivalent to a maximum likelihood procedure only in the presence of Gaussian noise. When this requirement is not satisfied, the regression is still valid, but the χ^2 values resulting from the fit will be distributed in a nontrivial way, rather than the χ^2 distribution expected in the case of Gaussian noise. Furthermore, the relationship between the covariance matrix of the
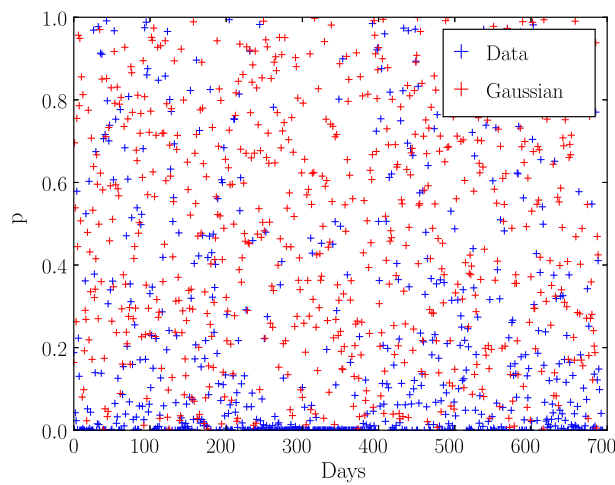
(a) Kolmogorov–Smirnov
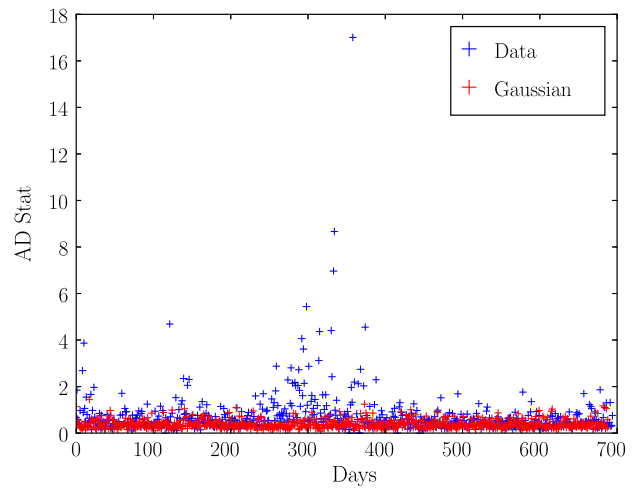
(b) Anderson–Darling

FIG. 15 (color online). Results of Gaussianity tests for daily segments of S5 H1 data prepared for the Crab (blue). The results for corresponding sets of Gaussian noise are presented for comparison (red).
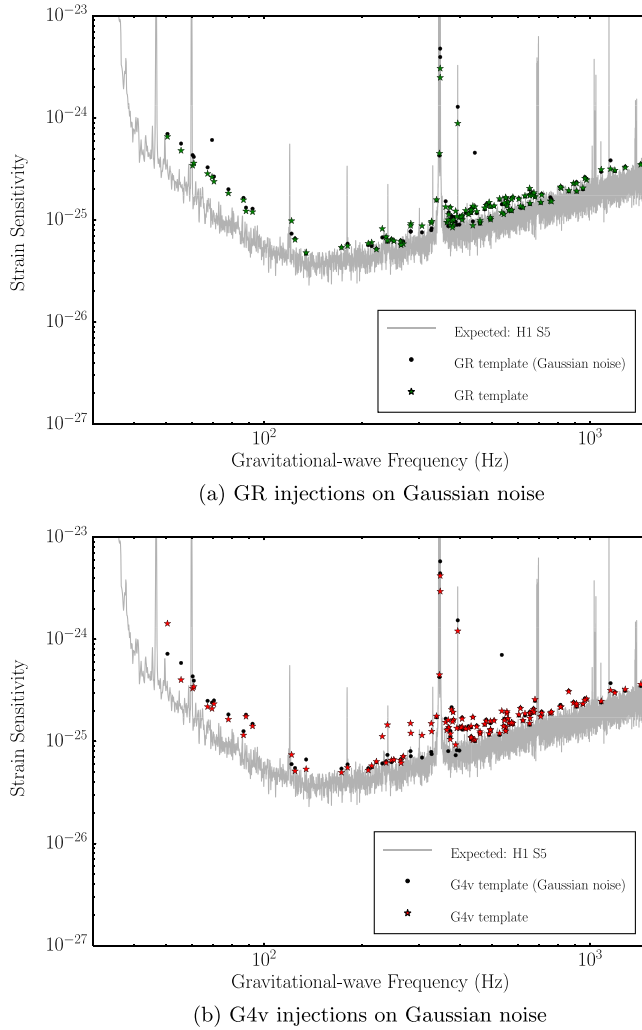
(a) GR injections on Gaussian noise

(b) G4v injections on Gaussian noise

FIG. 16 (color online). Expected sensitivity ($\alpha_\mathrm{n} = 99.9\%$, $\alpha_\mathrm{up} = 95.0\%$) vs GW frequency. Comparison between fabricated Gaussian noise and actual LIGO noise. Searches were made with semi-model-dependent templates, Eqs. (45) and (48). The colored stars correspond to actual LIGO H1 noise (cf. Fig. 11), while the black dots correspond to fabricated Gaussian noise.

system and the standard uncertainties of the recovered coefficients becomes unclear. Therefore, it is important to statistically characterize the data and understand the limitations of our assumption of Gaussianity.

When taken as a whole, LIGO detector noise does not conform to a *stationary* Gaussian distribution. This can be visually confirmed by means of a histogram, as shown in Fig. 14 for the case of S5 H1 data prepared for the Crab. The divergence from Gaussianity is evident from the long tails, seen most clearly in the log-*y* version of the plot. As expected, the data fail more rigorous standard Gaussianity tests, such as the Kolmogorov–Smirnov (KS) or the Anderson–Darling (AD) tests.

However, it is possible to split up the data into day-long (or shorter) segments, as was described in Sec. III B, so as to study the Gaussianity of the data on a day-to-day basis. The results of the KS and AD tests for each day segment, together with those for reference Gaussian noise series, are presented in Figs. 15(a) and 15(b), respectively. The KS test returns the *p* value for a null hypothesis that assumes the data are normally distributed; therefore, a lower *p* value implies a higher probability that the data are not Gaussian [30]. The AS test returns a figure of merit that is indirectly proportional to the significance with which the hypothesis of Gaussianity can be rejected; therefore, a higher AS statistic implies a higher probability that the data are not Gaussian [31].

It can be seen from the results of these tests that the statistical properties of the segments vary considerably from day to day. This could have been guessed from the nonstationarity of the data in Fig. 4, the daily variation of the standard deviation (Fig. 5), and other irregularities of the data. Nonetheless, most of the segments seem to pass the Gaussianity tests, with some remarkable exceptions around days 250–400 of the run. This corresponds to the spiking observed in the heterodyned data (GPS times 8.4×10^8–8.5×10^8 in Fig. 4).

To confirm that our assumption of Gaussianity is not too far from reality, we repeated our analysis (see Sec. V) on sets of synthetic Gaussian noise. To do this, for each pulsar, we generated streams of complex-valued data randomly selected from a normal distribution with the same standard deviation as the corresponding original LIGO data set. These series replaced the instantiations of reheterodyned data, but the search process was otherwise unchanged. The results of this comparison for S5 H1 are shown in Figs. 16, where we juxtaposed expected sensitivities obtained using Gaussian noise and actual LIGO noise (cf. Sec. V). These plots confirm that, indeed, we obtain qualitatively the same results with Gaussian noise as with actual LIGO data.

[1] C. M. Will, Living Rev. Relativity **17,** 4 (2014).
[2] S. G. Turyshev, Annu. Rev. Nucl. Part. Sci. **58,** 30 (2008).
[3] J. P. Ostriker and J. E. Gunn, Astrophys. J. **157,** 1395 (1969).
[4] I. Shklovskii, Sov. Astron. **13,** 562 (1970).
[5] G. M. Harry, Classical Quantum Gravity **27,** 084006 (2010).
[6] A. J. Weinstein, Classical Quantum Gravity **29,** 124012 (2012).

[7] W. Del Pozzo, J. Veitch, and A. Vecchio, Phys. Rev. D **83,** 082002 (2011).

[8] T. G. F. Li, W. Del Pozzo, S. Vitale, C. Van Den Broeck, M. Agathos, J. Veitch, K. Grover, T. Sidery, R. Sturani, and A. Vecchio, Phys. Rev. D **85,** 082003 (2012).

[9] M. Agathos, W. Del Pozzo, T. G. F. Li, C. Van Den Broeck, J. Veitch, and S. Vitale, Phys. Rev. D **89,** 082001 (2014).

[10] K. Chatziioannou, N. Yunes, and N. Cornish, Phys. Rev. D **86,** 022004 (2012).

[11] N. Yunes, R. O'Shaughnessy, B. J. Owen, and S. Alexander, Phys. Rev. D **82,** 064017 (2010).

[12] P. Hoava, A. Mohd, C. M. Melby-Thompson, and P. Shawhan, Gen. Relativ. Gravit. **46,** 1720 (2014).

[13] C. Mead, arXiv:1503.04866.

[14] M. Zimmermann and E. Szedenits, Phys. Rev. D **20,** 351 (1979).

[15] D. I. Jones and N. Andersson, Mon. Not. R. Astron. Soc. **331,** 203 (2002).

[16] W. Althouse, L. Jones, and A. Lazzarini, Report No. LIGO-T980044, 2001.

[17] B. Allen, arXiv:gr-qc/9607075.

[18] C. Ng and R. W. Romani, Astrophys. J. **673,** 411 (2008).

[19] R. T. Edwards, G. B. Hobbs, and R. N. Manchester, Mon. Not. R. Astron. Soc. **372,** 1549 (2006).

[20] R. Dupuis and G. Woan, Phys. Rev. D **72,** 102002 (2005).

[21] LIGO Scientific Collaboration and Virgo Collaboration, Astrophys. J. **713,** 671 (2010).

[22] A. Nishizawa, A. Taruya, K. Hayama, S. Kawamura, and M.-a. Sakagami, Phys. Rev. D **79,** 082002 (2009).

[23] A. Blaut, Phys. Rev. D **85,** 043005 (2012).

[24] T. M. Niebauer, A. Rüdiger, R. Schilling, L. Schnupp, W. Winkler, and K. Danzmann, Phys. Rev. D **47,** 3106 (1993).

[25] P. Astone, S. DAntonio, S. Frasca, and C. Palomba, Classical Quantum Gravity **27,** 194016 (2010).

[26] A. Olive *et al.* (Particle Data Group), Chin. Phys. C **38,** 090001 (2014).

[27] R. N. Manchester, G. B. Hobbs, A. Teoh, and M. Hobbs, Astron. J. **129,** 1993 (2005).

[28] LIGO Scientific Collaboration, Rep. Prog. Phys. **72,** 076901 (2009).

[29] M. Vallisneri, J. Kanner, R. Williams, A. Weinstein, and B. Stephens, *Proceedings of the 10th LISA Symposium, University of Florida, Gainsville* (IOP Publishing, Gainesville, Florida, 2014).

[30] I. M. Chakravarty, J. D. Roy, and R. G. Laha, *Handbook of Methods of Applied Statistics, Volume I* (Wiley, New York, 1967), p. 392.

[31] T. W. Anderson and D. A. Darling, Ann. Math. Stat. **23,** 193 (1952).